



HAL
open science

Topology-corrected segmentation and local intensity estimates for improved partial volume classification of brain cortex in MRI.

Andrea Rueda, Oscar Acosta, Michel Couprie, Pierrick Bourgeat, Jurgen Fripp, Nicholas Dowson, Eduardo Romero, Olivier Salvado

► To cite this version:

Andrea Rueda, Oscar Acosta, Michel Couprie, Pierrick Bourgeat, Jurgen Fripp, et al.. Topology-corrected segmentation and local intensity estimates for improved partial volume classification of brain cortex in MRI.. *Journal of Neuroscience Methods*, 2010, 188 (2), pp.305-315. 10.1016/j.jneumeth.2010.02.020 . inserm-00608891

HAL Id: inserm-00608891

<https://inserm.hal.science/inserm-00608891>

Submitted on 15 Jul 2011

HAL is a multi-disciplinary open access archive for the deposit and dissemination of scientific research documents, whether they are published or not. The documents may come from teaching and research institutions in France or abroad, or from public or private research centers.

L'archive ouverte pluridisciplinaire **HAL**, est destinée au dépôt et à la diffusion de documents scientifiques de niveau recherche, publiés ou non, émanant des établissements d'enseignement et de recherche français ou étrangers, des laboratoires publics ou privés.

Topology-corrected segmentation and local intensity estimates for improved partial volume classification of brain cortex in MRI

Andrea Rueda^{a,b}, Oscar Acosta^{a,d}, Michel Couprie^c, Pierrick Bourgeat^a,
Jurgen Fripp^a, Nicholas Dowson^a, Eduardo Romero^b, Olivier Salvado^a

^a*CSIRO Preventative Health National Research Flagship, ICTC, The Australian e-Health Research Centre - BioMedIA, Herston, Australia.*

^b*BioIngenium Research Group, Universidad Nacional de Colombia, Bogotá, Colombia*

^c*Université Paris-Est, Laboratoire d'Informatique Gaspard-Monge, ESIEE Paris, France*

^d*Laboratoire de Traitement du Signal et de l'Image (LTSI), INSERM U642, Université de Rennes 1, France.*

Abstract

In magnetic resonance imaging (MRI), accuracy and precision with which brain structures may be quantified are frequently affected by the partial volume (PV) effect. PV is due to the limited spatial resolution of MRI compared to the size of anatomical structures. Accurate classification of mixed voxels and correct estimation of the proportion of each pure tissue (fractional content) may help to increase the precision of cortical thickness estimation in regions where this measure is particularly difficult, such as deep sulci. The contribution of this work is twofold: on the one hand, we propose a new method to label voxels and compute tissue fractional content, integrating a mechanism for detecting sulci with topology preserving operators. On the other hand, we improve the computation of the fractional content of mixed voxels using local estimation of pure tissue intensity means. Accuracy and precision were assessed using simulated and real MR data and comparison with other existing approaches demonstrated the benefits of our method. Significant improvements in gray matter (GM) classification and

cortical thickness estimation were brought by the topology correction. The fractional content root mean squared error diminished by 6.3% ($p < 0.01$) on simulated data. The reproducibility error decreased by 8.8% ($p < 0.001$) and the Jaccard similarity measure increased by 3.5% on real data. Furthermore, compared with manually-guided expert segmentations, the similarity measure was improved by 12.0% ($p < 0.001$). Thickness estimation with the proposed method showed a higher reproducibility compared with the measure performed after partial volume classification using other methods.

Keywords: Brain tissue segmentation, Partial volume classification, Magnetic resonance imaging, Topology correction, Sulci detection, Cortical thickness estimation

1. Introduction

Accurate segmentation of Magnetic Resonance (MR) images into different brain tissues, namely gray matter (GM), white matter (WM), and cerebrospinal fluid (CSF), can allow *in-vivo* quantification of structural modifications appearing during neurodegenerative diseases. However, MR-related artifacts, such as intensity inhomogeneity, noise and partial volume (PV) effects, can hamper the precision of this task. Inhomogeneities can be characterized by a low frequency multiplicative bias field and are mostly due to the sensitivity of the receiver coils and, in some cases, to non-homogeneous tissue MR properties. The noise is Rician distributed and it has been shown to strongly affect the tissue classification (Van Leemput et al., 2003). Finally, PV effects appear when the size of anatomical features being imaged is comparable to the voxel size, causing blurring at the interfaces between tissues. In some cases, e.g. with opposed banks of GM in deep sulci, misclassification problems appear, affecting further processings such as cortical thickness estimation.

16 Topological operators and constraints have been widely used to correct
17 and achieve accurate cortical tissue segmentations (Ségonne, 2008; Bazin and
18 Pham, 2005; Han et al., 2002; Kriegeskorte and Goebel, 2001). It has been
19 assumed that the cerebral cortex is a folded sheet of GM built upon the
20 WM, which would have the topology of a hollow sphere if the midline hemi-
21 spheric connections were artificially removed. Due to MR artifacts, the seg-
22 mentation process cannot guarantee this assumption, generating deviations
23 from the true anatomy of the structures of interest. Proposed approaches
24 that address this issue can be classified in two categories: methods that in-
25 clude topological constraints directly into the segmentation process, based on
26 active contours (Ségonne, 2008), topology adaptive snakes (McInerney and
27 Terzopoulos, 1999), digital topology models (Bazin and Pham, 2005, 2007)
28 or segmentation by registration to an atlas (Kriegeskorte and Goebel, 2001);
29 and retrospective techniques that correct the topology after the segmentation
30 process (Han et al., 2002). Those approaches are focused on ameliorating the
31 topology of the segmented tissues, working directly on a voxel or on a mesh
32 (surface) space. Voxel-based methods operate directly on the volumetric tis-
33 sue segmentations, by removing or adding voxels according to topological
34 constraints. However, remotion or addition of a whole voxel in thin struc-
35 tures such as the GM may considerably modify the measure of thickness
36 (ranging between ± 1 voxel) if any mechanism such as partial volume is not
37 used to compensate for the structural modifications. In contrast, mesh-based
38 techniques requires an initial 3D reconstruction (triangular mesh) of the vol-
39 umetric segmentations. The approaches for segmentation and cortical thick-
40 ness estimation operating directly with the surfaces, such as CLASP (Kim
41 et al., 2005), BrainVISA (Mangin et al., 1995) or Freesurfer (Dale et al., 1999;
42 Fischl et al., 1999; Fischl and Dale, 2000), incorporate mechanisms to pre-

43 vent self-intersection of surfaces or topology correction, imposing also some
44 smoothness constraints. Mesh-based approaches are however computation-
45 ally more expensive, because of the needed additional reconstruction step.
46 Overall, after or during the mesh generation, most of the methods tackle the
47 elimination of tunnels and handles (Fischl et al., 1999; Florent Ségonne and
48 Fischl, 2007; Jaume et al., 2005; Zhou et al., 2007).

49 On the other hand, PV estimation has received considerable attention
50 in the last few years and different approaches have been proposed for clas-
51 sification and computation of fractional content (Santago and Gage, 1993;
52 Laidlaw et al., 1998; Shattuck et al., 2001; Noe and Gee, 2001; Van Leemput
53 et al., 2003; Tohka et al., 2004; Chiverton and Wells, 2008). Most techniques
54 model voxel intensity as a linear combination of the intensity distributions of
55 the possible tissue types within each voxel (Choi et al., 1991; Noe and Gee,
56 2001). Computing the fractional content of voxels therefore requires both
57 pure and mixed voxels to have been previously classified. Shattuck et al.
58 (2001) implemented a maximum *a posteriori* (MAP) classifier, which com-
59 bined a tissue measurement model with a prior model of the local spatial
60 interactions to obtain six tissue types: three pure and three mixed. The
61 fractional content for the mixed voxels was calculated based on the global in-
62 tensity mean of pure tissue types. Tohka et al. (2004) proposed an algorithm
63 which used statistical estimators, based on the MAP estimation (Shattuck
64 et al., 2001). Recently, Chiverton and Wells (2008) presented a local adaptive
65 Gradient-controlled spatial regularizer (GSR) using a Markov Random Field
66 to model the class membership and a Markov chain Monte Carlo (MCMC)
67 simulation to adapt the model to the observed data. The labelling error may
68 remain high because the intensity inhomogeneities (not explicitly modelled)
69 and the noise may lead to misdetection of mixed voxels mainly in tight sulci,

70 representing a portion of GM/CSF/GM within the same voxel.

71 The approaches previously presented have been focused on solving either
72 the PV estimation or the topology correction. Our contribution consists
73 in demonstrating that better results and performance are obtained if both
74 strategies are combined together with a spatial intensity variation modeling.
75 In this paper, we propose a new method aimed at improving both PV classi-
76 fication and fractional content computation, working at a voxel level in order
77 to be accurate and computationally efficient. The improved classification
78 is achieved by imposing topological constraints to the binary segmentation
79 and thus detecting hidden mixed voxels in zones of tight sulci. The accurate
80 fractional content estimation is attained by computing the fractional content
81 as a linear relation between robust local intensity averages of pure tissue
82 voxels. The spatially dependent averaging helps to overcome the problems
83 of intensity inhomogeneity for a given tissue across the image.

84 In the next section we describe our methods, followed by experiments
85 using simulated and real data. We also compare the results with other pre-
86 viously proposed methods. We demonstrated the utility of our approach by
87 integrating the whole process to our voxel-based cortical thickness estimation
88 pipeline.

89 **2. Methods**

90 The proposed strategy follows the steps depicted in Figure .1: Firstly, an
91 initial classification of voxels into pure tissues WM, GM and CSF and mixed
92 tissues WM/GM and GM/CSF is performed. Secondly, topology-constraints
93 are introduced in the classification assuming that the GM is a continuous
94 layer covering the WM. A topology preserving dilation of the WM over GM
95 adds robustness to the delineation of mixed voxels GM/CSF in deep sulci.

96 Finally, the estimation of fractional content for mixed voxels is adaptively
97 performed based on a local averaging of the pure tissue voxels.

98 INSERT FIGURE .1 HERE

99 2.1. Pure tissue segmentation

100 A first segmentation of pure brain tissues into GM, WM and CSF is per-
101 formed based on an implementation of the expectation-maximisation (EM)
102 segmentation method as in (Van Leemput et al., 1999). Here, the Colin atlas
103 and associated priors are first affinely registered to the data using a robust
104 block matching approach (Ourselin et al., 2001), followed by a diffeomorphic
105 Demons non-rigid registration (Vercauteren et al., 2007). Probabilistic tissue
106 maps associated with the atlas were used to initialize the EM segmentation
107 and enforce spatial consistency throughout the segmentation. The probabil-
108 ity density functions of the tissues are modelled with 6 Gaussians (WM, GM,
109 CSF and 3 for non brain tissues, skull and background). Finally, hard seg-
110 mentations are obtained after the EM segmentation by labelling each voxel
111 with the most probable tissue.

112 2.2. Initial partial volume labelling

113 Using the hard segmentations, a first labelling of partial volume voxels
114 are identified within the hard segmentations and along the interfaces of pure
115 tissues. Three pure tissue classes and two mixture classes are considered
116 $\Gamma = \{\text{GM, CSF, WM, CSF/GM, GM/WM}\}$. A maximum *a posteriori* classi-
117 fication (MAP) is made and labels the voxels as belonging to the set Γ . This
118 procedure, relying on both intensity and spatial information, extends the
119 method proposed by (Shattuck et al., 2001), but we assume that each voxel
120 contains at most two tissues (Santago and Gage, 1993), and PV classification
121 is restricted to the region formed by a dilated GM region (radius 2) because

122 only the cortical thickness is sought. To take into account dependency on the
123 neighbouring tissue types, a Markov prior that models local spatial interac-
124 tions was implemented using a Potts model in order to perform the labelling.
125 As in (Shattuck et al., 2001; Tohka et al., 2004; Kim et al., 2005), we use the
126 Iterated Conditional Modes (ICM) algorithm as explained in (Besag, 1986)
127 to search for the optimal labelled image. According to this, every voxel is
128 updated once per iteration until no label changes occur between iterations.
129 This model favors classification of contiguous regions of GM, WM and CSF
130 and encourages configurations of voxels that make physical sense such as
131 GM/CSF or GM/WM voxels adjacent to GM.

132 *2.3. A topology preserving segmentation*

133 After the MAP labelling, some of the sulci may be misdetected, as the
134 intensity of buried PV GM/CSF voxels is close to that of the GM. In order to
135 refine the segmentation and identify such buried GM/CSF voxels, we used a
136 homotopic dilation of the consolidated $\mathbf{WM} = \{\text{WM}, \text{WM/GM}\}$ constrained
137 by the GM, leading to a better delineation of deep sulci. To preserve this
138 folds during dilation, the set \mathbf{WM} is corrected first to assure that shares the
139 topology of a filled sphere.

140 The homotopic transformations that we used are topology-preserving pro-
141 cedures that consist of sequentially deleting or adding single points (voxels)
142 as described in (Bertrand and Malandain, 1994). The algorithms used are
143 detailed in Appendix A. Our topology preserving segmentation of the WM
144 consists in performing a homotopic dilation of a seed set of voxels, called \mathbf{S} ,
145 constrained to only add voxels from the set \mathbf{WM} , knowing that \mathbf{S} is topo-
146 logically equivalent to a filled sphere. The result of this operation is denoted
147 by \mathbf{SWM} . For example, \mathbf{S} could be made of single voxels chosen in the white
148 matter, but we describe below a way to obtain a seed that is closer to the

149 expected result, and thus leads to a more robust segmentation.

150 To obtain the seed \mathbf{S} , we first compute a surface skeleton \mathbf{SK} of \mathbf{WM} , by
151 dilating using Algorithm 2 as described in Appendix A. Then, we perform
152 an homotopic erosion, constrained by \mathbf{SK} , of a full cuboid that includes \mathbf{SK} .
153 Finally, we perform an homotopic dilation of the same seed set \mathbf{S} , constrained
154 by the set $\mathbf{SWM} \cup \mathbf{GM}$ to only add GM and WM voxels, and we subtract
155 \mathbf{SWM} from the result to obtain the corrected GM.

156 This method is performed on 3D sets, but for clarity we illustrate it on
157 a 2D reduced example in Figure .2. Notice that small black components in
158 Figure 2(b) can correspond to tunnels in the 3D image, thus simple connected
159 component filtering would not give the correct region. Figures .3 and .4 show
160 further examples in 3D.

161 INSERT FIGURE .2 HERE

162 INSERT FIGURE .3 HERE

163 INSERT FIGURE .4 HERE

164 *2.4. Partial volume relabelling and fractional content*

165 The main contribution of the topology is the relabelling of missegmented
166 GM voxels in hidden sulci as mixed GM/CSF. Once the topologically cor-
167 rected WM, GM, CSF, WM/GM and GM/CSF segmentations are obtained,
168 the portion of pure tissue, called here fractional content F , is computed for
169 each mixed voxel by estimating the local contribution of each pure tissue.
170 We assume that each voxel contains at most two tissues and the new la-
171 belling corresponds only to the mixed voxels WM/GM and GM/CSF. For
172 each mixed voxel, the fractional content F ranges between $[0, 1]$ depending
173 on the amount of pure tissue. Thus, for pure tissue voxels the fractional

174 content F_j are set to 1 for the class j and 0 otherwise. For mixed voxels
 175 ($x \in WM/GM, GM/CSF$), the fractional content $F_{j/k}$ between both pure
 176 tissues j and k is computed using the intensity $I(x)$ of the image and the
 177 robust local averages of the closest pure tissue voxels $\mu_j(x)$ and $\mu_k(x)$, such
 178 that:

$$F_{j/k}(x) = U \left(\frac{\mu_k(x) - I(x)}{\mu_k(x) - \mu_j(x)} \right) \quad (1)$$

179 where $U(\cdot)$ is a limiter restricting the range of the fractional content to $[0, 1]$.
 180 Unlike (Shattuck et al., 2001), which uses the same linear relation between
 181 global means of tissues to compute fractional content, we compute μ_k and μ_j
 182 as robust local averages rather than global means. This is done by computing
 183 the mean of the median 50% of pure tissue intensities (interquartile mean)
 184 within a $5mm$ radius sphere, thus rejecting local outliers, over a denoised
 185 version of the original MR image. The noise is removed by applying the
 186 optimized non-local means method proposed in (Coupe et al., 2008).

187 Pure tissue voxels are selected by eroding pure tissue segmentations using
 188 a $2mm$ radius, therefore reducing the influence of any mixed voxel. Finally,
 189 the computed averages are propagated back towards the location of the mixed
 190 voxels x , resulting in values of $\mu_j(x)$ and $\mu_k(x)$ that represent the average of
 191 the closest pure tissue voxels (Figure .5). The GM fractional content map
 192 is eventually defined as $F_{GM/WM} \cup F_{GM} \cup F_{GM/CSF}$. Using a robust local
 193 mean overcomes issues related to intensity inhomogeneities and variations of
 194 pure tissue signal across the image, weighting accordingly the signal when
 195 computing the fractional content.

196 INSERT FIGURE .5 HERE

197 INSERT FIGURE .6 HERE

198 Regional differences in the cell structure and the distribution of different
199 layers of the cortex result in variation of regional intensity differences for
200 the same tissue across the brain. These differences produces local variation
201 of contrast between the tissues that might be pronounced with ageing Salat
202 et al. (2009). Whereas global homogeneity assumptions will bias the voxel
203 fractional content estimation, a local computation of intensity averages for
204 pure tissue yields a more accurate value, which accounts for the changes in
205 cytoarchitecture visibles in MR. A local estimate allows also to overcome the
206 issues of intensity inhomogeneities due to the artifacts during the acquisition.

207 To illustrate the spatial differences in signal, GM intensity was measured
208 over the population of 20 young adults scans, acquired as described in Sub-
209 section 3.3. Figure .6 shows the local average intensity of GM across the
210 brain for an individual. In this example, precentral gyrus presented a higher
211 average value than the temporal or occipital lobe. The same pattern appear
212 in average in all the healthy individuals. The contrast between the tissues
213 has been also measured using the Equation 2 as

$$F_{Contrast} = \frac{\mu_{WM} - \mu_{GM}}{\mu_{GM} - \mu_{CSF}} \quad (2)$$

214 where μ_{WM} , μ_{GM} and μ_{CSF} are the regional averages of WM, GM and CSF
215 respectively, which can be considered as a measure of the contrast between
216 WM and GM normalized by the CSF. Figure .7 shows the regional differences
217 for the population of 20 young controls.

218 INSERT FIGURE .7 HERE

219 3. Experiments

220 To evaluate our method, named hereafter as Topologically-corrected Par-
221 tial Volume (TPV), we used different brain MR data sets including simulated
222 and real images. The purpose was twofold, firstly to illustrate the effect of the
223 topology correction in the estimation of fractional content for mixed voxels,
224 and secondly to compare the obtained results with those publicly available in
225 the area. After that, the method was integrated to our voxel-based cortical
226 thickness estimation pipeline. Experiments demonstrated that the overall
227 method showed a better estimate of thickness and a high reproducibility on
228 real data.

229 *3.1. Simulated MR data*

230 A set of 15 simulated MR brain images was obtained from the BrainWeb
231 Simulated Brain Database, maintained by the McConnell Brain Imaging Cen-
232 tre at the Montreal Neurological Institute (Cocosco et al., 1997) and avail-
233 able at www.bic.mni.mcgill.ca/brainweb. Each simulation was a $1mm^3$
234 isotropic T1-weighted MRI volume with dimensions $181 \times 217 \times 181$, gen-
235 erated with varying noise level and intensity inhomogeneity. We tested our
236 method on each combination of 1%, 3%, 5%, 7% or 9% noise levels together
237 with 0%, 20% or 40% intensity nonuniformities. BrainWeb also provides the
238 fuzzy tissue membership volumes, one for each tissue class, together with a
239 discrete anatomical model of the simulated normal brain.

240 *3.2. Manually segmented real MR data*

241 20 normal MR brain data sets and their manual segmentations were ob-
242 tained from the Internet Brain Segmentation Repository (IBSR), provided
243 by the Center for Morphometric Analysis at Massachusetts General Hospi-
244 tal and available at www.cma.mgh.harvard.edu/ibsr. The data sets were
245 acquired along the coronal axis with slice dimension of 256×256 and $1mm^2$

246 resolution. Interslice distance is $3mm$ and the number of slices for each vol-
247 ume varies between 60 and 65. The data sets have various levels of artifacts,
248 as low contrast and relatively large intensity gradients, that further affects
249 performance of the algorithm. CMA also provides expert tissue labellings of
250 each brain into WM, GM, and CSF, together with reference similarity values
251 for some classification techniques.

252 *3.3. Cross sectional series of real MR scans*

253 20 young healthy subjects (12 female, 8 male; age between 19 - 34 years),
254 who underwent 4 scans at baseline and 4 more scans during a subsequent
255 session after a short delay (less than 90 days), were randomly selected from
256 the Open Access Series of Imaging Studies (OASIS) database (Marcus et al.,
257 2007), available at www.oasis-brains.org. For each session, an average
258 motion-corrected image (co-registered average of all available data) was used
259 for our tests. The scans were T1-weighted Magnetization Prepared RApid
260 Gradient Echo (MP-RAGE) in sagittal orientation with isotropic $1mm^3$ res-
261 olution ($256 \times 256 \times 128$ pixels). This data was used to assess the precision of
262 the method when classifying partial volume voxels. We also tested the robust-
263 ness when the method was integrated in our voxel-based cortical thickness
264 estimation pipeline (Acosta et al., 2009), particularly when the detection of
265 deep sulci was improved.

266 *3.4. Error and similarity measures*

To quantitatively evaluate performance of the method over both simu-
lated and real MR data sets and compare these results with other well-known
results, we used two different metrics: the root mean square (RMS) error for
comparison of PV classification maps, and the Jaccard similarity measure for
comparison of the corresponding crisp tissue segmentations. The RMS error

was used to quantify the differences between the fractional content calculated for each tissue and the corresponding values in the ground truth fuzzy membership images. As in (Shattuck et al., 2001), the RMS error between two images X and Y is calculated as

$$e_{RMS}(X, Y) = \sqrt{\frac{1}{|\Omega|} \sum_{k \in \Omega} |y_k - x_k|^2}$$

where Ω is the brain region, x_k and y_k are the image intensities at position k .

The Jaccard similarity metric, also known as the Tanimoto coefficient, measures the amount of overlap (agreement) between two images X and Y by taking the ratio between the size of their intersection and the size of their union:

$$J(X, Y) = \frac{|X \cap Y|}{|X \cup Y|}$$

This metric yields values between 0 and 1, where 0 means complete dissimilarity and 1 stands for identical images.

4. Results and discussion

4.1. BrainWeb

Performance of our TPV method was firstly assessed on the simulated brain images from BrainWeb. One example of the resulting PV maps for WM, GM and CSF, compared with the available ground truth, on the synthetic brain volume, 3% noise level and 20% bias field, is depicted in Figure .8. Comparisons between our method and a classical MAP approach are shown in Figure .9 for the computed GMPVC fractional content map. It must be noted that compared to a classical MAP approach as in (Shattuck et al., 2001), the sulci were better delineated by introducing the topological constraints (Figure 9(g)). In this example, a deep sulci voxel with similar intensity to the average GM, will be classified as GM and not as a mixed GM/CSF voxel

282 unless anatomical constraints are introduced. The mean RMS error of frac-
283 tional content over the entire BrainWeb data set significantly decreased to
284 6.1% ($p < 0.01$) for the obtained GMPVC map, as compared with the results
285 reported in (Shattuck et al., 2001). Overall, a good agreement was shown
286 between the computed PV maps and the ground truth, available as fuzzy
287 tissue membership volumes. RMS errors for different noise and intensity
288 nonuniformity levels are shown in Table .1. As expected, the computed error
289 was robust to the bias field, which additionally validates the local averaging
290 approach rather than the global one.

291 INSERT FIGURE .8 HERE

292 INSERT FIGURE .9 HERE

293 INSERT TABLE .1 HERE

294 The variability between different regions in the brain may affect the per-
295 formance of PV classifiers (Chiverton and Wells, 2008). To illustrate this
296 effect, we used the automated anatomical labeling (AAL) template (Tzourio-
297 Mazoyer et al., 2002) to calculate the RMS error within each region as
298 in (Chiverton and Wells, 2008). Averaged results for different levels of noise
299 are shown in Figure .10. As a low variability with respect to the bias field
300 was observed, the depicted value corresponds to the average over all the bias
301 field levels (0%, 20% and 40%). The smallest errors appeared in the amyg-
302 dala (42xx), the insula (30xx), the supplementary motor area (24xx) and
303 the olfactory (25xx); while lower agreement was found in the basal ganglia
304 (70xx), the middle occipital (52xx) and the parietal superior (61xx).

305 INSERT FIGURE .10 HERE

306

INSERT FIGURE .11 HERE

307 We also compared our TPV method with the results reported by Chiver-
308 ton and Wells (2008) (GSR) and Shattuck et al. (2001) (SMAP). The results
309 are depicted in Figure .11. Evidence suggests that the local average intensity
310 strategy makes the classification more robust to bias field variations, and on
311 average performs better than other methods for low levels of noise (1% to
312 7%) and bias field of 20%. We point out the fact that GSR does not explic-
313 itly take into account the bias field, hence its effect appears in the reported
314 results.

315 *4.2. Real MR Data*

316 *4.2.1. OASIS*

317 The reproducibility was measured by applying the method to two of the
318 MR scans from the same individual from the OASIS database. We compared
319 the results with the MAP classifier as in (Shattuck et al., 2001). Significant
320 improvements in GM PV estimation were brought by the topology correc-
321 tion. The reproducibility error decreased by 8.8% in GM and 8.5% in WM
322 ($p < 0.001$), measured as the RMS between the PV maps obtained on the
323 rigidly registered baseline and repeat scans. Likewise, when comparing the
324 crisp segmentations obtained by thresholding by 0.5 the baseline and repeat
325 GM PV maps, the Jaccard similarity measure increased by 3.5% in GM. To
326 compute crisp segmentations, each mixed voxel was assigned to the tissue
327 class with the highest fractional content and the obtained segmentation were
328 subsequently compared.

329 *4.2.2. IBSR*

330 Our method was also compared with both TMCD (trimmed minimum
331 covariance determinant) (Tohka et al., 2004) and MMC (mixture model clus-

332 tering) (Noe and Gee, 2001) on the IBSR data sets. Since the ground truth
333 is available as manual segmentations performed by clinical experts, we com-
334 pared the segmentations obtained from the crisped PV maps. Figure .12
335 shows an example of the ground truth provided by IBSR and a hard segmen-
336 tation calculated after applying our method. Figure 13(b) depicts the results
337 of the comparison for the GM in the 20 normal subjects. As in (Chiverton
338 and Wells, 2008), results of manual expert segmentation and pure tissue class-
339 sification presented by Ibrahim et al. (2006) (HMM, hidden Markov model)
340 were included for reference. Significant improvements in GM classification
341 were demonstrated using the TPV, compared to a MAP classifier. The sim-
342 ilarity measure (Jaccard) was improved by 8.7% in GM and 2.6% in WM
343 ($p < 0.001$).

344 INSERT FIGURE .12 HERE

345 Poor similarity results were obtained in 5 cases, which exhibited strong
346 shading artifacts that impeded a reliable GM and WM classification. Simi-
347 lar findings were presented in (Noe and Gee, 2001), who excluded them from
348 the analysis. We also observed that the anisotropy in the images biased the
349 computation of the local averages. Table .2 summarizes the mean (\pm stan-
350 dard deviation) of the Jaccard similarity values for each method, excluding
351 the volumes with too severe intensity inhomogeneity. In average, our TPV
352 method performed better for WM and GM compared to the others, except-
353 ing averaged GM segmentation against (Noe and Gee, 2001). It must be
354 noted that when the PV maps were used to generate the crisp segmenta-
355 tions, the mixed GM/CSF voxels in deep sulci with fractional content above
356 0.5 might be wrongly reclassified as GM. Under those conditions, the con-
357 tribution of topology correction in the segmentation can not be fully and

358 accurately validated with this experiment. Nonetheless, we report these re-
359 sults for completeness.

360 INSERT TABLE .2 HERE

361 INSERT FIGURE .13 HERE

362 *4.3. Computational performance*

363 On each image of the BrainWeb data set, after the initial MAP segmenta-
364 tion, the topology correction and PV fractional content estimation takes less
365 than 10 minutes. For the OASIS data sets, the procedure takes about 9 min-
366 utes, while for the IBSR images the topology correction and PV fractional
367 content estimation takes less than 4 minutes. Operations were encoded in a
368 single-thread application and then executed in a standard Intel Core 2 Duo
369 (3.00GHz, 2 GB RAM) machine running Linux.

370 *4.4. Deep sulci cutting and cortical thickness estimation on real data*

371 We integrated the proposed sulci detection and improved partial volume
372 classification methods to our cortical thickness estimation pipeline (Acosta
373 et al., 2009), as depicted in Figure .14. Then, we computed the thickness, at
374 two different acquisition times, for the same 20 young healthy subjects from
375 the OASIS database (Marcus et al., 2007) used in the experiment described
376 in Section 3.3. The reproducibility was assessed by using the Pearson cor-
377 relation coefficient for each Region Of Interest (ROI) of the AAL template
378 (Tzourio-Mazoyer et al., 2002), excluding the cerebellum and subcortical *nu-*
379 *clei* from the analysis.

380 INSERT FIGURE .14 HERE

381 Thickness estimation with the proposed method (TPV) showed a higher
382 reproducibility compared with the measure performed after partial volume
383 classification using (Shattuck et al., 2001). As can be seen in Figure .15, the
384 differences in cortical thickness between scans were reduced after applying the
385 TPV. The Pearson correlation coefficient was 0.915 in average and a paired t-
386 test did not reveal any significant differences between the two measurements
387 ($p < 0.1$). Also, the difference between scans was decreased by 13.7% in
388 average, as shown in Table .3.

389 INSERT FIGURE .15 HERE

390 INSERT TABLE .3 HERE

391 By using the proposed method, we found a mean (\pm std. dev.) cortical
392 thickness over the whole brain of $2.08mm$ (± 0.11) for all the subjects, which
393 is within the accepted range of cortical thickness for healthy young adults.
394 In previous studies, when the PV is not taken into account as in (Yezzi
395 and Prince, 2003), the computed mean thickness for the same population
396 was $4.69mm$ (± 0.11). And when the PV classification method proposed
397 by (Shattuck et al., 2001) is used, without any topology correction, the com-
398 puted mean thickness was $3.06mm$ (± 0.25); using those same PV maps, but
399 correcting the topology problems, decreases the mean thickness to $2.75mm$
400 (± 0.17).

401 INSERT FIGURE .16 HERE

402 Fig. .16 depicts in histograms the impact of the topology correction and
403 the accurate PV estimation on the cortical thickness calculation task. The
404 higher thickness values produced after the first PV classification disappeared
405 when the topology of GM is corrected and the accurate PV value is computed

406 with the TPV. Fig. 16(a) shows the histogram of the average thickness for
407 the 20 MR subjects before any topological modifications, after the topology
408 correction and with TPV. Fig. 16(b) depicts the differences for each of the
409 cortical thickness histograms between Step 1 and Step 2, illustrating the
410 improvement after the TPV. The number of voxels above $4mm$ in average
411 has been dramatically reduced. Fig. 16(c) shows the differences between
412 topology corrections and TPV, in average in this further step the number of
413 voxels above $2.5mm$ has been reduced.

414 5. Conclusion

415 We have described a simple and fast technique to improve PV estimation
416 of brain tissues from T1W MRI. It improves the detection of hidden mixed
417 voxels in deep sulci by correcting for the topology errors in the segmentation
418 and uses local averages to better estimate the fractional content. We show
419 that fractional tissue content estimation can be improved for low levels of
420 noise and regardless the intensity inhomogeneity, resulting in superior brain
421 tissue segmentations.

422 Topology correction improved the classification of mixed voxels in op-
423 posed banks of buried sulci by assuming GM as a continuous layer following
424 the WM, with the topology of a filled sphere. Local modelling of tissue inten-
425 sities helps to overcome the issues related with local intensity inhomogeneity
426 and tissue MR properties across the image. Even with a preprocessing stage
427 to correct the intensity inhomogeneities, pure cortical tissues show differ-
428 ent intensity levels in the MRI. This suggests that the tissue properties are
429 different depending on the region of the brain. Accuracy and precision were
430 demonstrated and comparisons with other methods showed comparative per-
431 formance with simulated and real MR data.

432 We demonstrated the usefulness of the method to improve the accuracy
433 of the cortical thickness estimation. By labelling mixed GM/CSF voxels in
434 deep sulci and by recomputing a spatially compensated PV map, the measure
435 of thickness in difficult regions is improved. Our method showed a high
436 reproducibility on real data, with an extremely good agreement between the
437 baseline and repeat scans. The computed values of thickness for young adults
438 are similar to the ones reported previously in the literature. In the future,
439 we plan to use our technique on clinical data to study cortical atrophy in
440 Alzheimer's disease and other neurodegenerative diseases. We intend also to
441 develop voxel-based techniques for inter-subject comparisons, a challenging
442 issue given the large anatomical variability between patients.

443 AppendixA

444 Topology preservation and homotopic transformations

445

446 Homotopic transformations are topology-preserving procedures that con-
447 sist of sequentially deleting or adding *simple points*. This operation works
448 only on binary images, such as the pure tissue segmentations, where each
449 voxel is considered as a point. Informally, a simple point of an object X is a
450 point that can be added or removed from X without changing the topological
451 characteristics of X . It is possible to locally characterize simple points in 3D
452 using two *topological numbers* T and Tb (Bertrand and Malandain, 1994).

453 Thus, skipping some technical details, let $A(x)$ be the set of points of
454 $X \setminus \{x\}$ lying in a neighborhood of x , and let $Ab(x)$ be the set of points of
455 the complement of X (background) lying in a neighborhood of x . Then, $T(x)$
456 (resp. $Tb(x)$) is the number of connected components of $A(x)$ (resp. $Ab(x)$).
457 A point x is simple if and only if $T(x) = Tb(x) = 1$. Topological numbers
458 are useful for classifying points of an object X based on local topological
459 characteristics: for example, a point x such that $Tb(x) > 1$ characterizes
460 a region of the object which separates (locally) its background into several
461 parts.

462 Based on these notions, given an object X , a subset I of X and a priority
463 function P , Algorithm 1 computes an *homotopic erosion of X constrained by*
464 I , that is, an object that is topologically equivalent to X , that contains I and
465 that has no simple point outside I . In this algorithm, the priority function
466 P is usually chosen as the inverse of the distance to I , in order to select in
467 the first place the points that are farthest to the set I . This choice will be
468 assumed in the remaining operations.

469 Applying Algorithm 1 to the complementary sets of X and I , then in-

Algorithm 1 Homotopic erosion of X constrained by I

repeatSelect $x \in X \setminus I$ such that $P(x)$ is minimal**if** x is simple for X **then** $X = X \setminus \{x\}$ **end if****until** stability

470 verting the result, yields an *homotopic dilation of X constrained by I* . In a
471 similar way, Algorithm 2 (Bertrand and Couprie, 2007) computes a *surface*
472 *skeleton of X* which contains medial surfaces of the original object (provided
that the priority function P is a distance map of X).

Algorithm 2 Surface skeleton of X

Let C be a null image**repeat**Select $x \in X$ such that x is simple for X , $C(x) == \emptyset$ and $P(x)$ is
minimal $X = X \setminus \{x\}$ **for** all y in the neighborhood of x **do****if** $Tb(y) > 1$ **then** $C(y) = 1$ **end if****end for****until** stability

473

474 **References**

- 475 Acosta, O., Bourgeat, P., Zuluaga, M. A., Fripp, J., Salvado, O., Ourselin,
476 S., 2009. Automated voxel-based 3D cortical thickness measurement in a
477 combined lagrangian-eulerian PDE approach using partial volume maps.
478 *Medical Image Analysis* 13, 730–743.
- 479 Bazin, P.-L., Pham, D. L., 2005. Topology correction using fast marching
480 methods and its application to brain segmentation. In: *Medical Image*
481 *Computing and Computer-Assisted Intervention 2005*. Lecture Notes in
482 *Computer Science*. Springer Verlag, pp. 484 – 491.
- 483 Bazin, P.-L., Pham, D. L., 2007. Topology-preserving tissue classification of
484 magnetic resonance brain images. *IEEE Transactions on Medical Imaging*
485 26 (4), 487–496.
- 486 Bertrand, G., Couprie, M., 2007. Transformations topologiques discrètes. In:
487 Coeurjolly, D., Montanvert, A., Chassery, J.-M. (Eds.), *Géométrie discrète*
488 *et images numériques*. Hermès, pp. 187–209.
- 489 Bertrand, G., Malandain, G., 1994. A new characterization of three-
490 dimensional simple points. *Pattern Recognition Letters* 15 (2), 169–175.
- 491 Besag, J., 1986. On the statistical analysis of dirty pictures. *Journal of the*
492 *Royal Statistical Society* 48, 259–302.
- 493 Chiverton, J., Wells, K., 2008. Adaptive partial volume classification of mri
494 data. *Physics in Medicine and Biology* 53 (20), 5577–5594.
- 495 Choi, H., Haynor, D., Kim, Y., 1991. Partial volume tissue classification of
496 multichannel magnetic resonance images - a mixel model. *IEEE Transac-*
497 *tions on Medical Imaging* 10 (3), 395–407.

- 498 Cocosco, C., Kollokian, V., Kwan, R.-S., Evans, A., 1997. Brainweb: Online
499 interface to a 3D MRI simulated brain database. *NeuroImage* 5 (4), S425.
- 500 Coupe, P., Yger, P., Prima, S., Hellier, P., Kervrann, C., Barillot, C., 2008.
501 An optimized blockwise nonlocal means denoising filter for 3-d magnetic
502 resonance images. *IEEE Transactions on Medical Imaging* 27 (4), 425–441.
- 503 Dale, A., Fischl, B., Sereno, M., 1999. Cortical surface-based analysis I:
504 Segmentation and surface reconstruction. *NeuroImage* 9 (2), 179–194.
- 505 Fischl, B., Dale, A., 2000. Measuring the thickness of the human cerebral cor-
506 tex from magnetic resonance images. *Proceedings of the National Academy
507 of Sciences of the United States of America* 97 (20), 11050–11055.
- 508 Fischl, B., Sereno, M., Dale, A., 1999. Cortical Surface-Based Analysis II: In-
509 flation, Flattening, and a Surface-Based Coordinate System. *NeuroImage*,
510 195–207.
- 511 Florent Ségonne, J. P., Fischl, B., 2007. Geometrically accurate topology-
512 correction of cortical surfaces using nonseparating loops. *IEEE Transac-
513 tions on Medical ImaginG* 26 (4), 518–529.
- 514 Han, X., Xu, C., Braga-Neto, U., Prince, J., 2002. Topology correction in
515 brain cortex segmentation using a multiscale, graph-based algorithm. *IEEE
516 Transactions on Medical Imaging* 21 (2), 109–121.
- 517 Ibrahim, M., John, N., Kabuka, M., Younis, A., 2006. Hidden markov
518 models-based 3d mri brain segmentation. *Image and Vision Computing*
519 24 (10), 1065–1079.
- 520 Jaume, S., Rondao, P., Macq, B., 2005. Open Topology: A Toolkit for Brain
521 Isosurface Correction. In: *MICCAI Open Source Workshop*.

- 522 Kim, J., Singh, V., Lee, J., Lerch, J., Ad-Dab'bagh, Y., MacDonald, D., Lee,
523 J., Kim, S., Evans, A., 2005. Automated 3D extraction and evaluation of
524 the inner and outer cortical surfaces using a Laplacian map and partial
525 volume effect classification. *NeuroImage* 27 (1), 210–221.
- 526 Kriegeskorte, N., Goebel, R., 2001. An efficient algorithm for topologically
527 correct segmentation of the cortical sheet in anatomical mr volumes. *Neu-
528 roimage* 14, 329–346.
- 529 Laidlaw, D., Fleischer, K., Barr, A., 1998. Partial-volume Bayesian classi-
530 fication of material mixtures in MR volume data using voxel histograms.
531 *IEEE Transactions on Medical Imaging* 17 (1), 74–86.
- 532 Mangin, J.-F., Frouin, V., Bloch, I., Régis, J., López-Krahe, J., 1995. From
533 3D magnetic resonance images to structural representations of the cortex
534 topography using topology preserving deformations. *Journal of Mathemat-
535 ical Imaging and Vision* 5 (4), 297–318.
- 536 Marcus, D. S., Wang, T. H., Parker, J., Csernansky1, J. G., C., M. J.,
537 L., B. R., 2007. Open access series of imaging studies (OASIS): Cross-
538 sectional MRI data in young, middle aged, nondemented, and demented
539 older adults. *Journal of Cognitive Neuroscience* 19, 1498–1507.
- 540 McInerney, T., Terzopoulos, D., 1999. Topology Adaptive Deformable Sur-
541 faces for Medical Image Volume Segmentation. *IEEE Transactions on Med-
542 ical Imaging* 18 (10), 840–850.
- 543 Noe, A., Gee, J., 2001. Partial volume segmentation of cerebral MRI scans
544 with mixture model clustering. In: *International Conference on Informa-
545 tion Processing in Medical Imaging*. Vol. 2082 of LNCS. Springer, pp.
546 423–430.

- 547 Ourselin, S., Roche, A., Subsol, G., Pennec, X., Ayache, N., 2001. Recon-
548 structing a 3D structure from serial histological sections. *Image and Vision*
549 *Computing* 19 (1), 25–31.
- 550 Salat, D.H., Lee, S.Y., van der Kouwe, A.J., Greve, D.N., Fischl, B., Rosas,
551 H.D., 2009. Age-associated alterations in cortical gray and white matter
552 signal intensity and gray to white matter contrast. *NeuroImage* 48 (1),
553 21–28.
- 554 Santago, P., Gage, H., 1993. Quantification of MR brain images by mix-
555 ture density and partial volume modeling. *IEEE Transactions on Medical*
556 *Imaging* 12 (3), 566–574.
- 557 Ségonne, F., 2008. Active contours under topology control - genus preserving
558 level sets. *International Journal of Computer Vision* 79 (2), 107 – 117.
- 559 Shattuck, D., Sandor-Leahy, S., Schaper, K., Rottenberg, D., Leahy, R.,
560 2001. Magnetic resonance image tissue classification using a partial volume
561 model. *Neuroimage* 13 (5), 856–876.
- 562 Tohka, J., Zijdenbos, A., Evans, A., 2004. Fast and robust parameter esti-
563 mation for statistical partial volume models in brain MRI. *NeuroImage*
564 23 (1), 84–97.
- 565 Tzourio-Mazoyer, N., Landeau, B., Papathanassiou, D., Crivello, F., Etard,
566 O., Delcroix, N., Mazoyer, B., Joliot, M., 2002. Automated anatomical
567 labeling of activations in spm using a macroscopic anatomical parcellation
568 of the mni mri single-subject brain. *NeuroImage* 15 (1), 273–289.
- 569 Van Leemput, K., Maes, F., Vandermeulan, D., Suetens, P., 1999. Auto-

- 570 mated model-based bias field correction of MR images of the brain. IEEE
571 Transactions on Medical Imaging 18 (10), 885–896.
- 572 Van Leemput, K., Maes, F., Vandermeulen, D., Suetens, P., 2003. A unifying
573 framework for partial volume segmentation of brain MR images. IEEE
574 Transactions on Medical Imaging 22 (1), 105–119.
- 575 Vercauteren, T., Pennec, X., Perchant, A., Ayache, N., 2007. Non-parametric
576 diffeomorphic image resgistration with the demons algorithm. In: Medi-
577 cal Image Computing and Computer-Assisted Intervention. Vol. 4792 of
578 LNCS. Springer Berlin / Heidelberg, Brisbane, Australia, pp. 319–326.
- 579 Yezzi, A.J., Prince, J.L., 2003. An Eulerian PDE approach for computing
580 tissue thickness. IEEE Transactions on Medical Imaging 22 (10), 1332–
581 1339.
- 582 Zhou, Q.-Y., Ju, T., Hu, S.-M., 2007. Topology repair of solid models using
583 skeletons. IEEE Transactions on Visualization and Computer Graphics
584 13 (4), 675–685.

		Intensity inhomogeneity					
		0%		20%		40%	
Noise		WM	GM	WM	GM	WM	GM
1%		0.129	0.130	0.129	0.131	0.125	0.132
3%		0.139	0.142	0.140	0.141	0.140	0.142
5%		0.174	0.174	0.172	0.171	0.170	0.171
7%		0.214	0.216	0.210	0.213	0.208	0.212
9%		0.251	0.261	0.245	0.258	0.242	0.256

Table .1: Fractional content RMS error on BrainWeb.

	MMC (Noe and Gee, 2001)	TMCD (Tohka et al., 2004)	TPV
WM	0.648 (\pm 0.198)	0.696 (\pm 0.050)	0.701 (\pm 0.042)
GM	0.753 (\pm 0.120)	0.697 (\pm 0.064)	0.708 (\pm 0.045)

Table .2: Mean (\pm standard deviation) of Jaccard similarity index for each method.

Brain lobule	Correlation coefficient		Differences between scans	
	SMAP	TPV	SMAP	TPV
Frontal	0.922	0.930	0.090	0.090
Limbic	0.901	0.883	0.158	0.121
Occipital	0.902	0.904	0.101	0.063
Parietal	0.906	0.920	0.058	0.060
Temporal	0.932	0.938	0.105	0.106
Average	0.912	0.915	0.102	0.088

Table .3: Pearson correlation coefficient and differences between scans for the OASIS dataset, grouped by brain lobules.

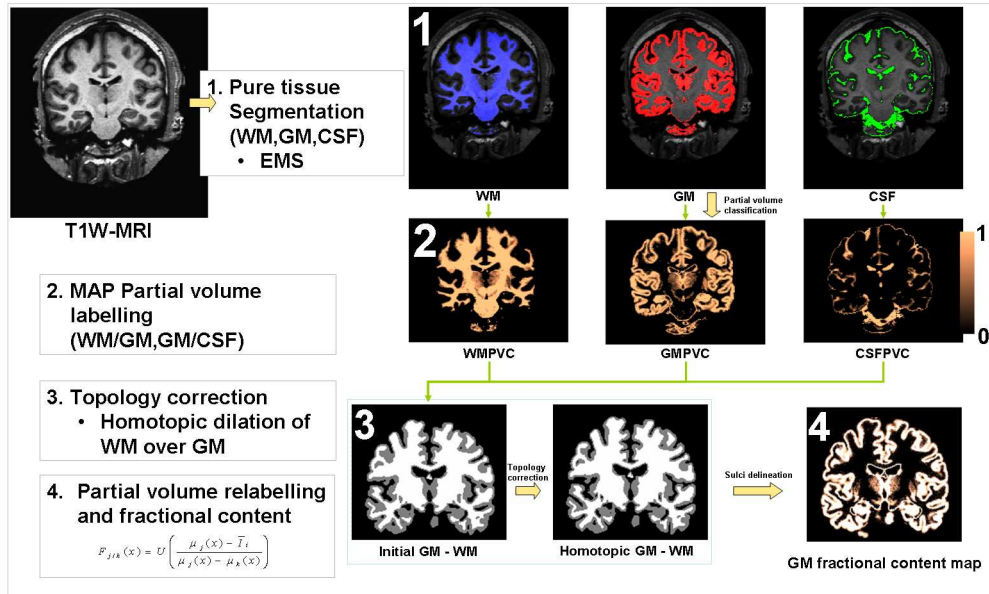


Figure .1: Overall process for topology-corrected PV estimation in MR images

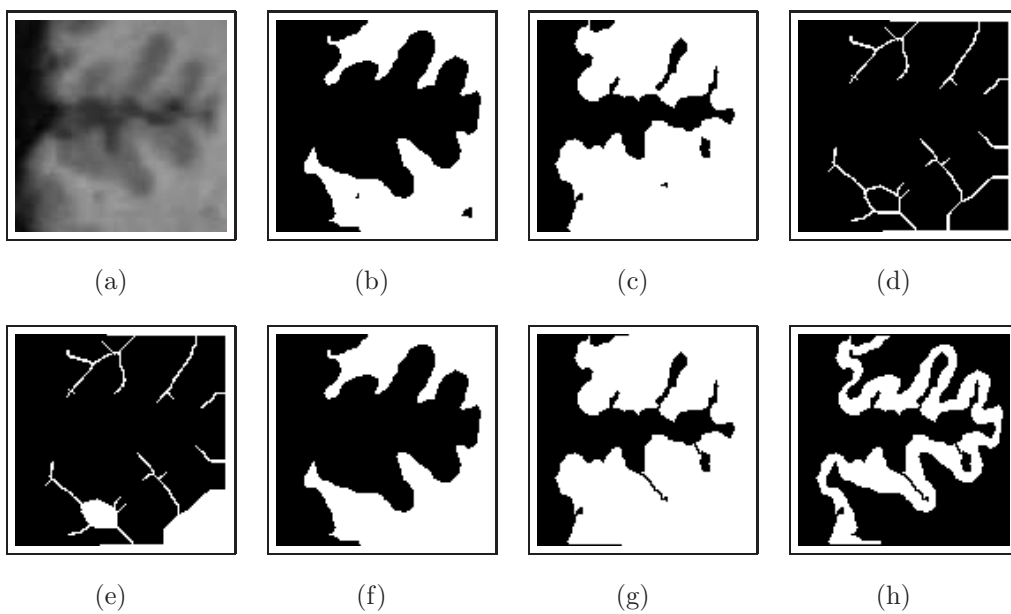


Figure .2: (a): original grayscale image. (b): segmented white matter (set \mathbf{WM}). (c): segmented white and gray matter (set $\mathbf{WM} \cup \mathbf{GM}$). (d): surface skeleton of \mathbf{WM} (set \mathbf{SK}). (e): seed set (set \mathbf{S}). (f): corrected white matter (set \mathbf{SWM}). (g): corrected white and gray matter formed by further homotopic dilation. (h): corrected gray matter (final result) formed by subtracted images (g) and (f).

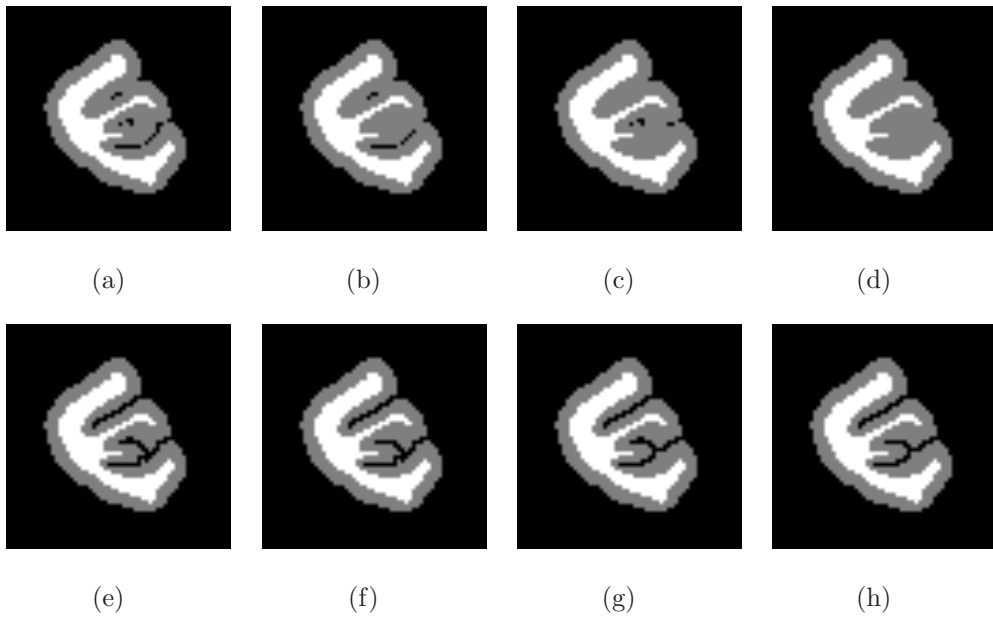


Figure .3: First row (a) - (d): Different initial configurations of a synthetic phantom. Second row (e) - (h): Corresponding topologically corrected WM-GM segmentations.

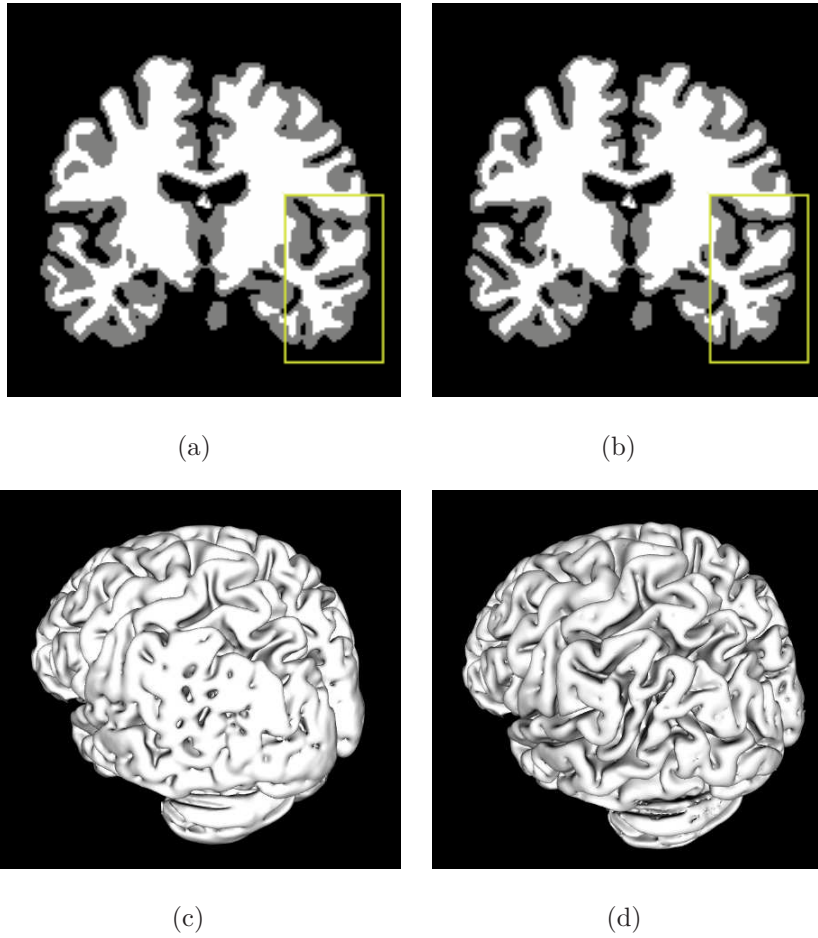


Figure .4: (a) Initial and (b) topologically corrected WM-GM segmentations, highlighted within the rectangle; (c) marching cubes reconstruction of GM before and (d) after the topology correction procedure.

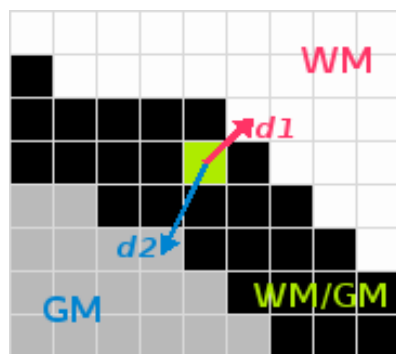


Figure .5: Schematic view of the local tissue averages for a given mixed voxel, where $d1$ and $d2$ relates to the closest voxels in the pure tissues.

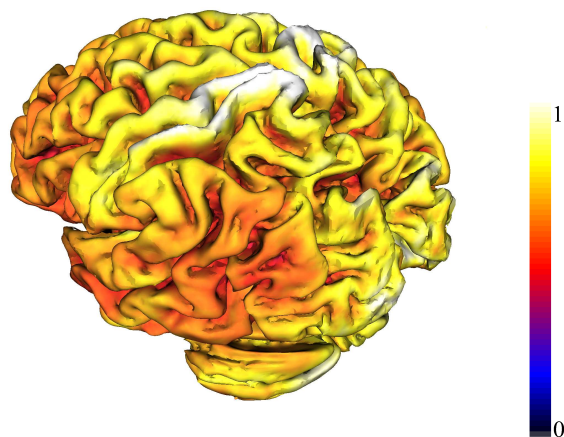


Figure .6: Averaged intensity within the connected components of the pure GM, computed as the interquartile mean (IQM) within a $5mm$ radius sphere on an OASIS example data, normalized by the Maximum of intensity. The differences between the regions clearly appear. Thus, GM tissue intensity will be different between the regions and global homogeneity assumptions will slightly bias the computation of partial volume.

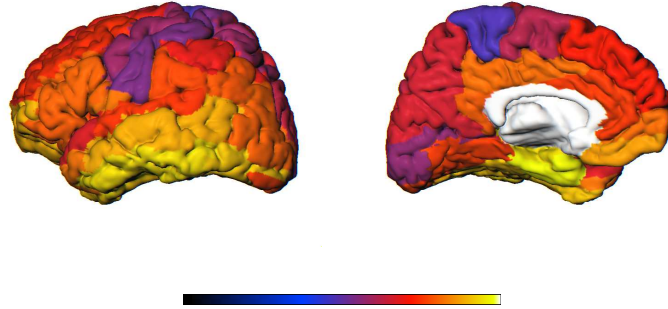


Figure .7: AAL template showing the regional differences in contrast between WM and GM over the surface, by calculating the ratio $\frac{\mu_{WM} - \mu_{GM}}{\mu_{GM} - \mu_{CSF}}$. Darkest colours indicate bigger ratios, light colours indicate small values. Left: lateral and Right: medial views.

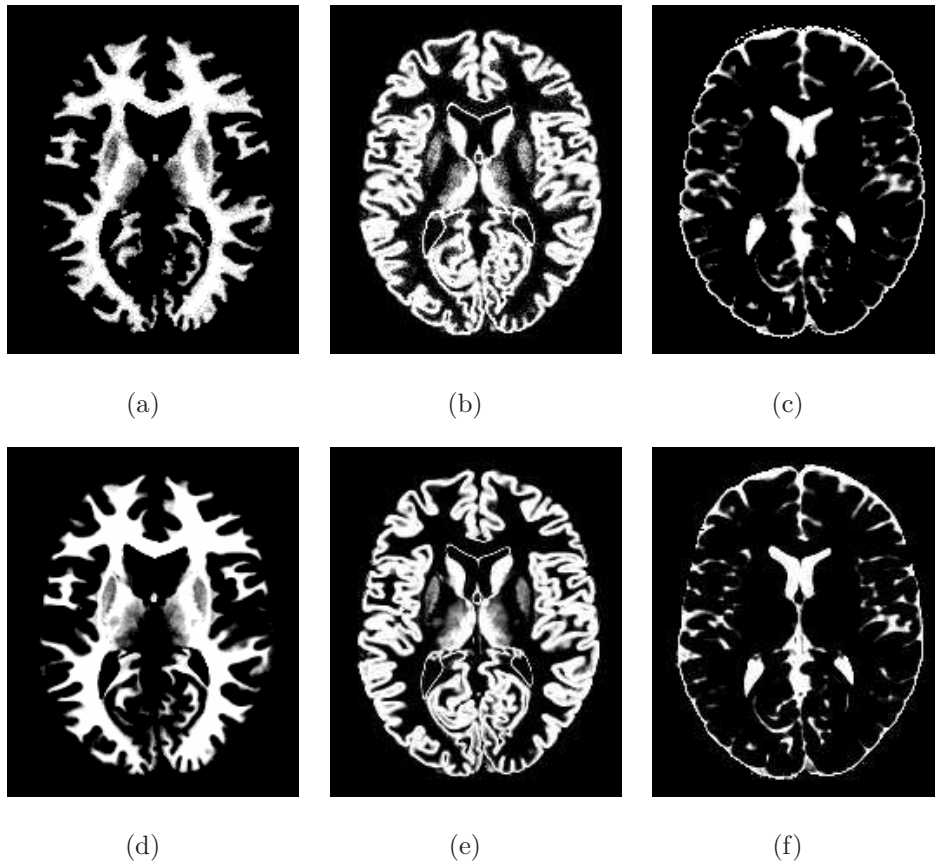


Figure .8: Partial volume segmentation of a simulated BrainWeb volume (3% noise, 20% bias field). PV maps for (a) WM, (b), GM (c) and CSF. Ground truth: (d) WM, (e), GM and (f) CSF.

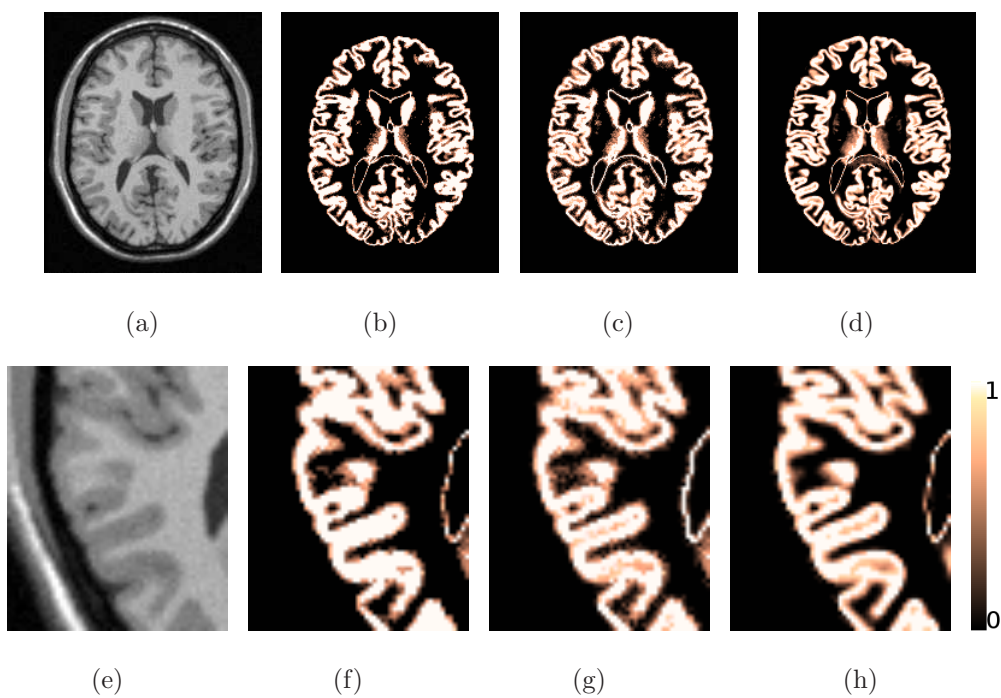
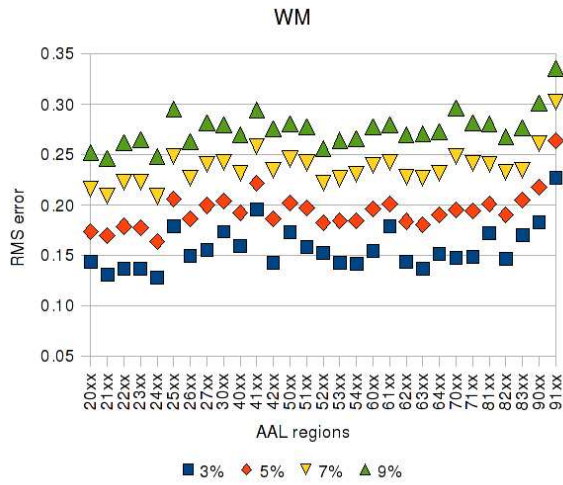
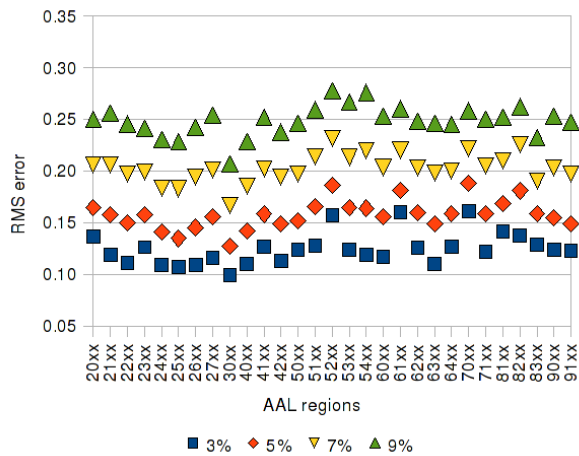


Figure .9: Example of PV estimation of a simulated BrainWeb volume (3% noise, 20% bias field). (a),(e) Original image, (b),(f) MAP PV estimation, (c),(g) Topologically-corrected PV, (a),(h) ground truth. In the detailed views we can observe the improvement in deep sulci, (g) relative to (f), brought by the topology correction.

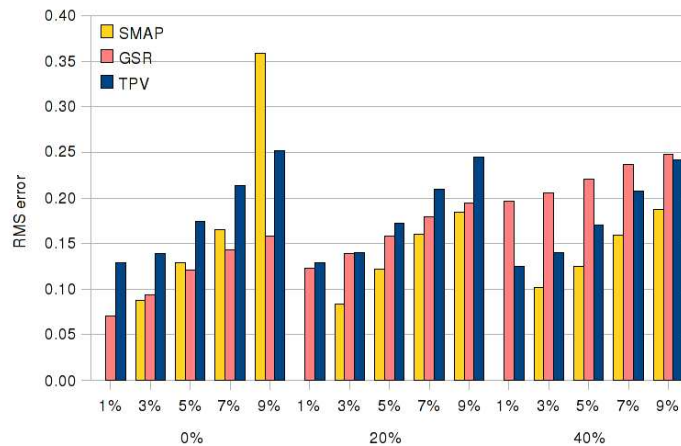


(a) WM

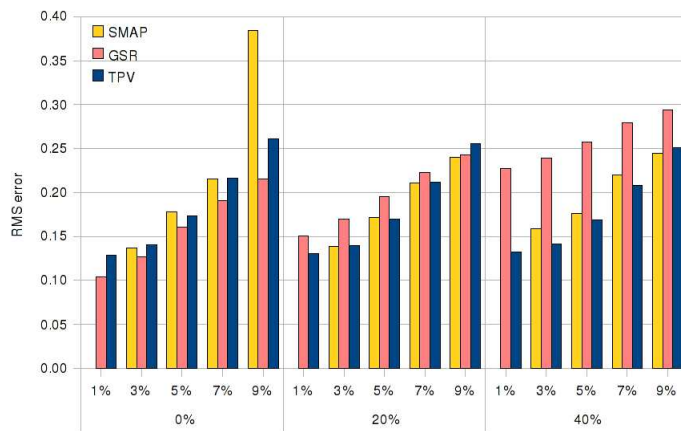


(b) GM

Figure .10: RMS error per AAL region (a) WM and (b) GM regions, for different noise levels using the same labels as (Chiverton and Wells, 2008).



(a) WM



(b) GM

Figure .11: PV estimation errors for (a) WM and (b) GM on BrainWeb, for different noise and bias field levels. (SMAP results for 1% noise not publicly available)

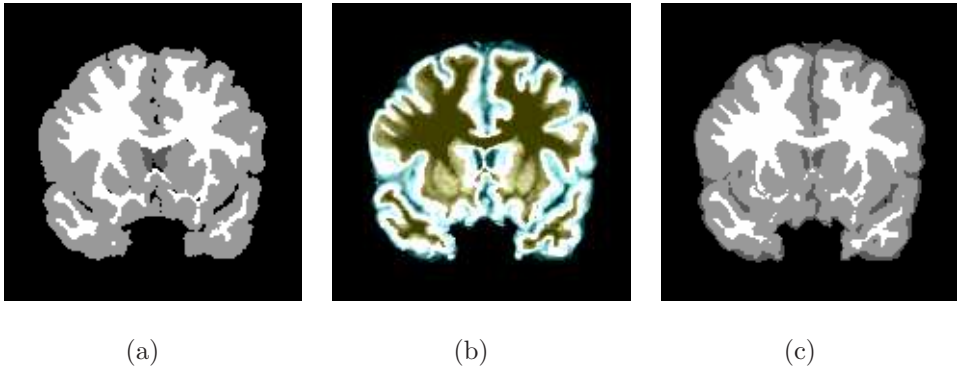
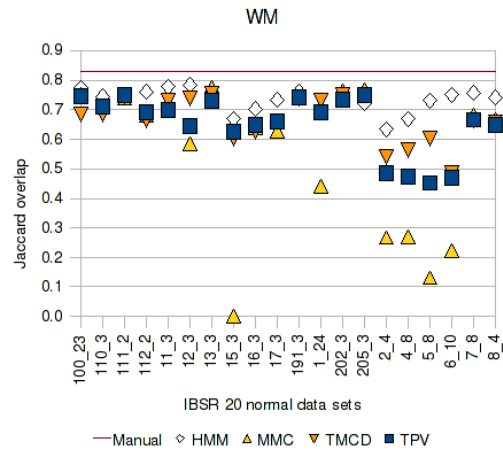
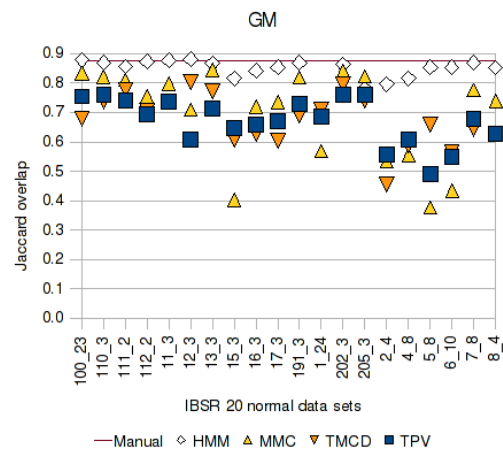


Figure .12: (a) IBSR Ground truth pure tissue classification. (b) Estimated PV maps (blue: GM/CSF, white: GM, yellow: GM/WM) and (c) computed crisp segmentation.



(a) WM



(b) GM

Figure .13: Jaccard similarity results for WM (a) and GM (b).

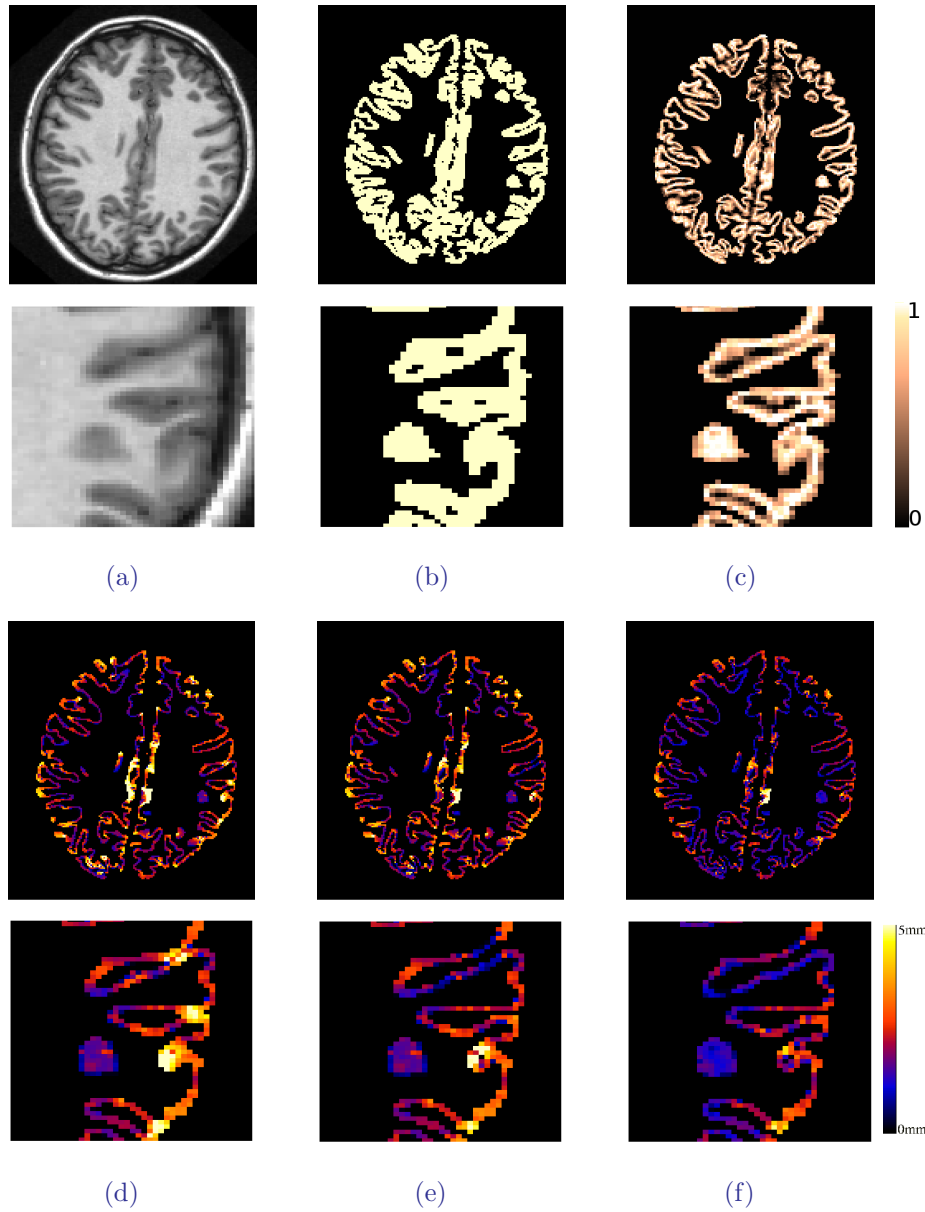


Figure .14: Example of cortical thickness estimation from MR. (a) Original T1-W MRI, (b) GM segmentation, (c) Topologically-corrected GM PV map. Cortical thickness maps (d) without any topology modifications, (e) after topology correction only, (f) after TPV. In the detailed views we can observe the improvement brought by the topology to delineate deep sulci zones, which allows an accurate measurement of the cortical thickness.

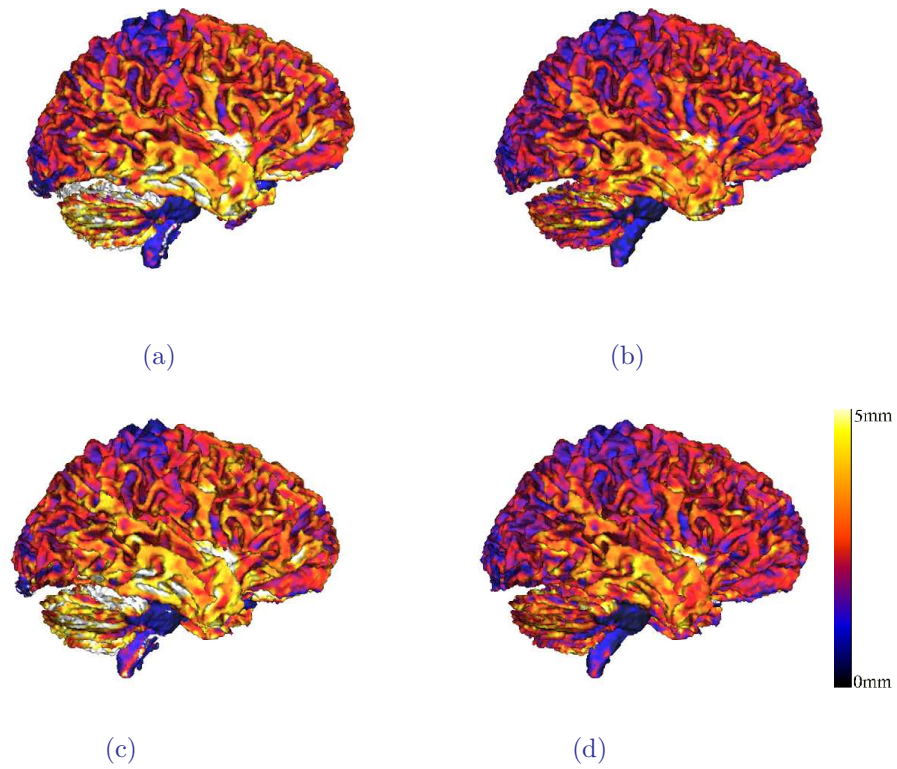


Figure .15: Surface representation of cortical thickness, computed at different steps for two scans of a single subject (OASIS). *Top row: Scan 1, Bottom row: Scan 2.* (a),(c) Without topology modifications, and (b),(d) with topologically-corrected GM PV map (TPV). Overall, we can observe the high values of thickness corrected with the TPV method.

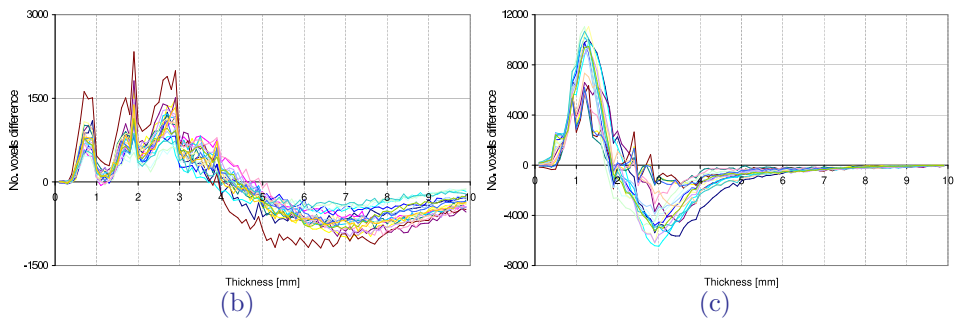
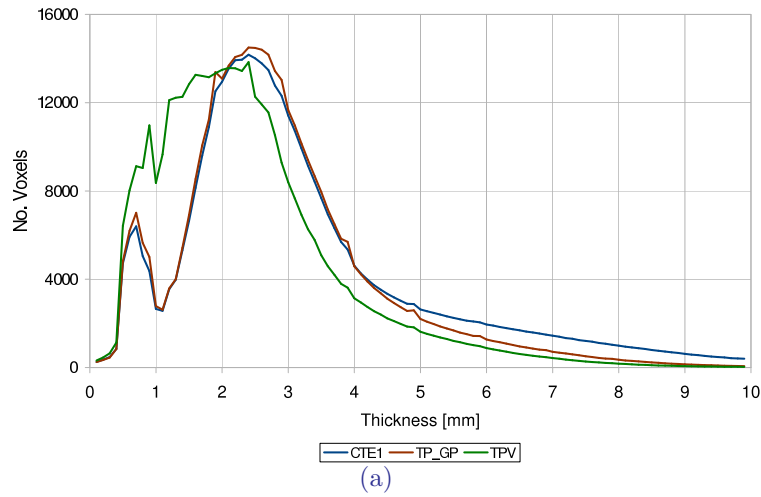


Figure .16: (a) Histogram of the average thickness for the 20 MR before topology correction (step 1), after topology correction (step 2) and with TPV. It is shown how the number of higher thickness voxels was reduced. (b) Differences in cortical thickness histograms between steps 1 and 2 for the 20 MR. This figure depicts the improvement after the topology. The number of voxels above 4mm in average has been dramatically reduced. (c) Differences between topology and TPV, in average the number of voxels above 2.5mm has been reduced consolidating the average thickness around 2.5mm (typical value for young adults).